12A.7

AIRBORNE DOPPLER RADAR AND DROPSONDE ANALYSIS OF AN OCEANIC COLD FRONT

Roger M. Wakimoto*
National Center for Atmospheric Research
Boulder, CO 80305

Hanne V. Murphey
UCLA
Los Angeles, CA 90095

1. INTRODUCTION

The Bergen School in Norway provided the first conceptualization of the evolution of fronts within an extratropical cyclone. Subsequently, numerous studies have endeavored to understand the dynamics and observational structure of these discontinuities since they are the focus of a significant fraction of the cyclone's precipitation and rapid changes in weather. Fronts also provide an environment for instabilities that may be responsible for generating smaller-scale weather phenomena. Most of the literature has focused on cold fronts largely as a result of the large horizontal temperature gradients, abrupt wind shifts and temperature changes, and their frequent association with severe weather (e.g., Browning and Harrold 1970, Hobbs and Biswas 1979, James and Browning 1979, Carbone 1982, Hobbs and Persson 1982, Ogura and Portis 1982, Young and Johnson 1984, Shapiro et al. 1985, Bond and Shapiro 1991, Locatelli et al. 1995).

Detailed and near simultaneous observations of cold fronts have been difficult to obtain owing to its long cross-frontal dimension spanning hundreds of kilometers and its depth which can encompass most of the troposphere. Accordingly, most past studies have focused on a small segment of the front or have made restrictive, steady-state assumptions during the data collection period. In addition, it is challenging to collect comprehensive data on the kinematic wind field while also accurately defining the thermodynamic structure of the front.

This paper presents an analysis of an oceanic cold front based on data collected by an airborne Doppler radar during the Fronts and Atlantic Storm Track Experiment (FASTEX; Joly et al. 1997) Intensive Observation Period (IOP) 11 on 5 – 6 February 1997. A research aircraft equipped with a Doppler radar flew several legs (~200 km in length) in the cross-frontal direction providing a detailed vertical cross section of its kinematic structure. This synthesized windfield was significantly enhanced by a series of dropsondes released by a second aircraft flying a parallel track at a higher altitude.

2. FASTEX AND THE AIRBORNE PLATFORMS

The field phase of FASTEX occurred in January and February 1997. The data set collected during the experiment was intended to help improve forecasts of end-of-storm-track cyclogenesis over the northeastern Atlantic Ocean (Joly et al. 1997). While there were a number of scientific objectives, the analysis in this paper focuses on the goal to document the mesoscale organization of cyclone cloud systems.

Two primary platforms used in the present study are the National Oceanic and Atmospheric Administration (NOAA) P-3 and the C-130 operated by the United Kingdom Met Office. The P-3 and the C-130 were deployed from Shannon, Ireland, and Lyneham, England, respectively. The C-130 was equipped to release dropsondes at regularly spaced intervals from altitudes between 6 and 8 km MSL (above mean sea level; hereafter, all heights are MSL). The dropsondes were rapidly deployed and led to horizontal spacing as small as 19 km with an average spacing of 30 km.

3. OVERVIEW OF IOP 11 AND THE P-3/C-130 FLIGHT TRACKS

The incipient upper-level trough and surface low associated with IOP 11 organized on 3-4 February over the western Atlantic Ocean (not shown). Subsequently, the entire system rapidly intensified as it moved eastward into the FASTEX domain. The surface cyclone was associated with its lowest central pressure (<984 mb) at 6 February 0000 UTC (hereafter; all times are UTC) as shown in Fig. 1a.

Flight tracks for the two aircraft were designed during the pre-IOP 11 planning meetings. The P-3 flew primarily at an attitude between 2-3 km and executed four approximately perpendicular penetrations through the frontal surface (Figs. 1b). The tracks plotted on the figure are ground-relative and were near the central low pressure of the cyclone. The flight plans for the C-130 were designed such that the dropsondes would be deployed along a path that was parallel to the P-3 tracks. This is well illustrated by the time-space adjusted aircraft tracks shown in Fig. 2 using a frontal motion 9.3 m s^{-1} from 300^{o}.

4. STRUCTURE OF THE COLD FRONT

The dual-Doppler synthesis of the ground-relative winds at 400 m from 0250–0325 is presented in Fig. 3. The precipitation echoes associated with the front were weak and scattered throughout the region. A linear band of echo is collocated with the front with maximum reflectivity values <30 dBZ.

* *Corresponding author address: Roger M. Wakimoto, National Center for Atmospheric Research, P.O. Box 3000, Boulder, CO 80307; e-mail: wakimoto@ucar.edu*

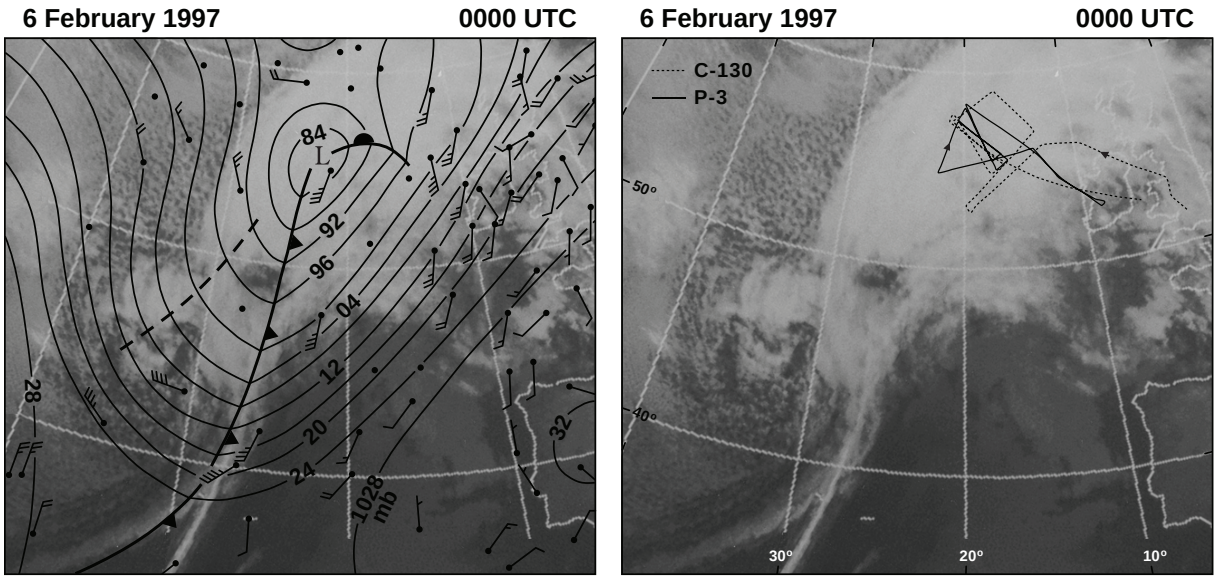

Fig 1. (a) Surface analyses and b) P-3 and C-130 flight tracks superimposed on top of the infrared satellite image at 0000 UTC 6 February 1997.

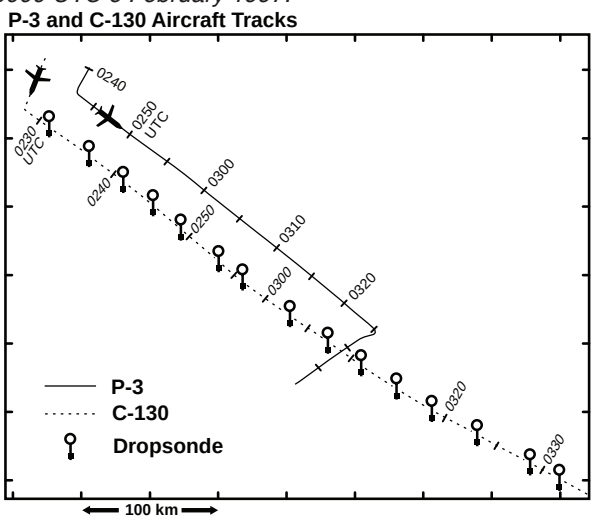

Fig. 2. Time-space adjusted aircraft tracks for the NOAA P-3 (black line) and C-130 (dashed line). The locations of the dropsondes deployed by the C-130 are shown.

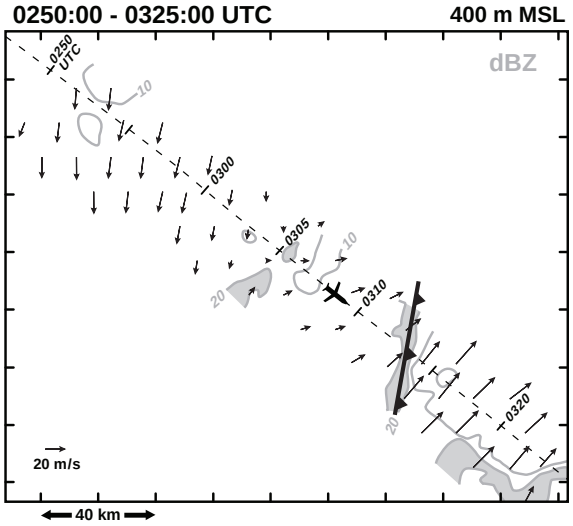

Fig. 3. Dual-Doppler wind syntheses from 0250:00 - 0325:00 UTC 6 February 1997 at 400 m MSL. Ground-relative winds superimposed on to radar reflectivity.

A vertical cross section was created that was oriented approximately perpendicular to the cold front. The dual-Doppler wind synthesis was rotated such that the abscissa was parallel to the front and the ordinate was pointed into the post-frontal cold air. The cross sections for each grid point along the abscissa were averaged (i.e., a total of 27 cross sections over a distance of 40 km).

The gray wind vectors in Fig. 4 highlight the dual-Doppler wind synthesis. The kinematic boundary of the cold front is well defined by the shift in wind direction from northerly within the post-frontal cold air to southwesterly flow in the warm sector (Fig. 4a). The front is also apparent in the sloping isopleths of virtual potential temperature (θ_v) over the polar air mass. The mixing ratio analysis reveals the relatively moist and dry air ahead of and behind the front, respectively.

Also apparent in the mixing ratio plot is an elevated pocket of dry air located 100-200 km ahead of the front. The dry pocket in Fig. 4a is located in a region of slight warming (indicated by the dashed line) suggesting that the dry air is a result of descending air. The absence of strong convection in the analysis region effectively discounts forced descent as a causal mechanism on this day. Low equivalent potential temperatures are also apparent in this region producing a region of potential instability (Fig. 4b). This type of thermodynamic structure could support pre-frontal convective activity although none was observed on this day.

There were weak positive vertical velocities near the leading edge of the cold front between the dropsondes deployed at 0253 and 0257 (Fig. 4b). The maximum updrafts speeds (>2 m s^{-1}) were noted ~75 km in post-frontal air mass and were positioned near a wave-like pattern in isopleths in θ_E (note the 308 and 310 K isopleths near the dropsonde deployed at 0249). A similar feature in the θ_E field can be identified along

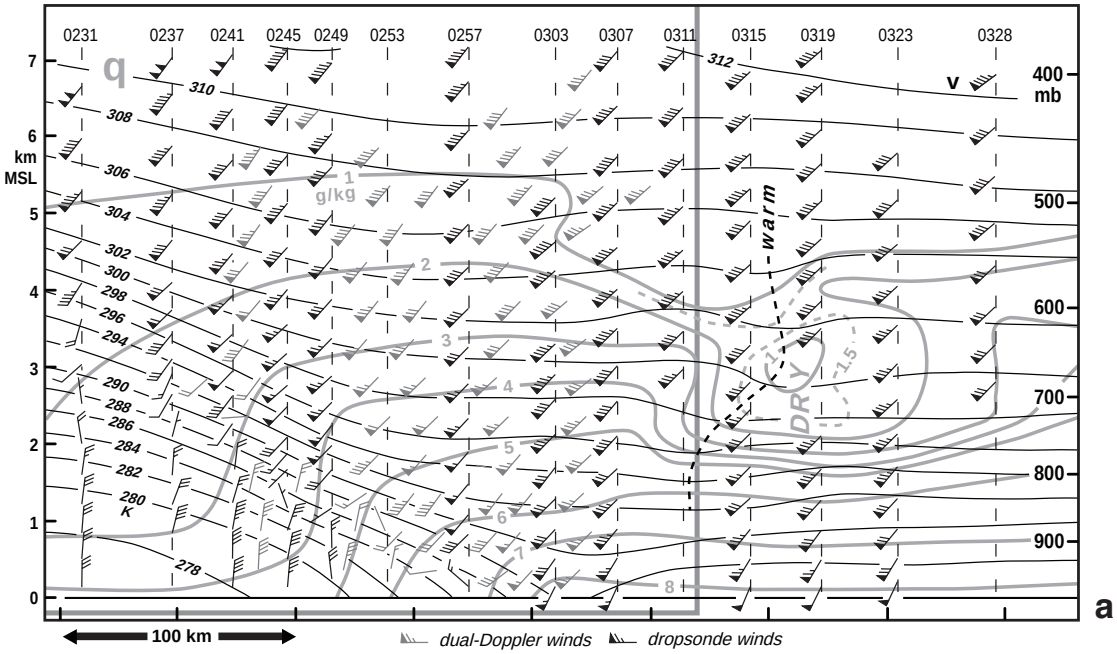

Fig. 4. Vertical cross section of dropsonde data through the cold front from 0231 to 0328 UTC on 6 February 1997. Ground-relative winds from the dropsonde and dual-Doppler synthesis (plotted as gray wind vectors) superimposed onto (a) virtual potential temperature and mixing ratio. (b) Equivalent potential temperature and vertical velocities derived from the Doppler synthesis. (c) Ageostrophic component of the wind parallel to the cold front and the gradient of the virtual potential temperature. Positive values of u_{ag} are into the figure. The large gray box is the dual-Doppler analysis region and is enlarged in Fig. 5.

the 310 K isopleth near the 0241 dropsonde location. Interestingly, the latter is also associated with an updraft region. Such features have been noted before and have been attributed to precipitation bands forming as a result of slantwise convection or gravity waves generated during frontogenesis (e.g., Emanuel 1983, Parsons and Hobbs 1983, Wolfsberg et al. 1986, Gall et al. 1988). Precipitation bands will be shown to exist near these updraft regions in a subsequent analysis.

The degree of geostrophic balance of the flow parallel to the front was estimated by calculating the ageostrophic wind ($u_{ag} = u - u_g$; see Fig. 4c). A large region of supergeostrophic flow is evident in the warm sector. The supergeostrophic nature of the upper-level jet stream located at levels >4 km near the soundings deployed at 0231 and 0237 is also noted.

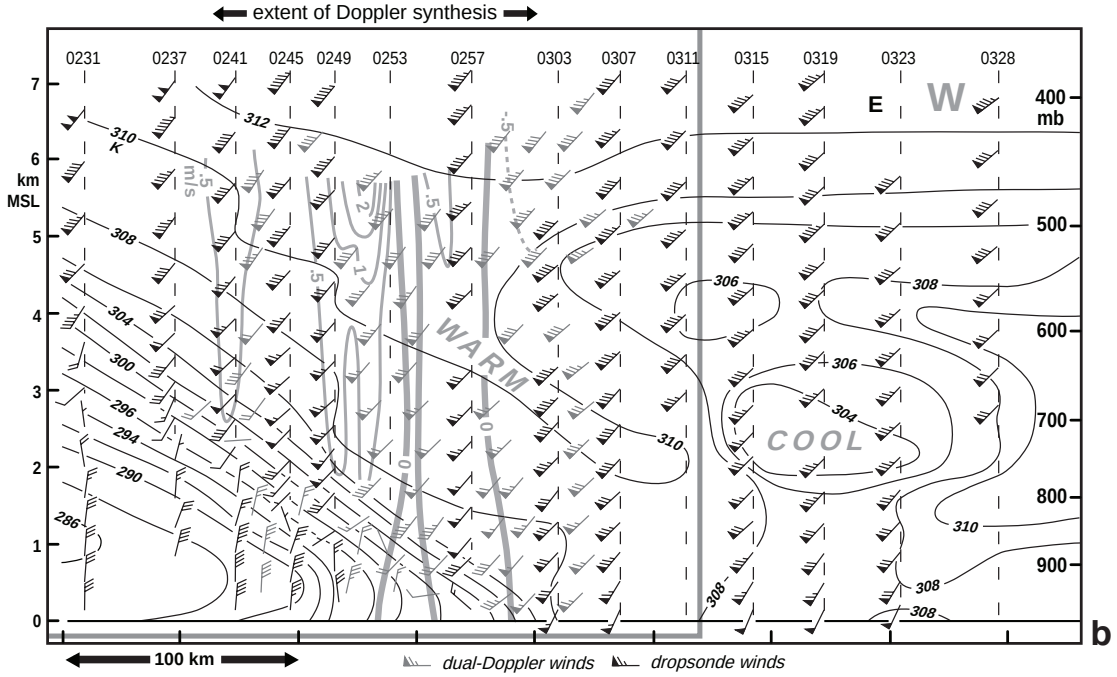

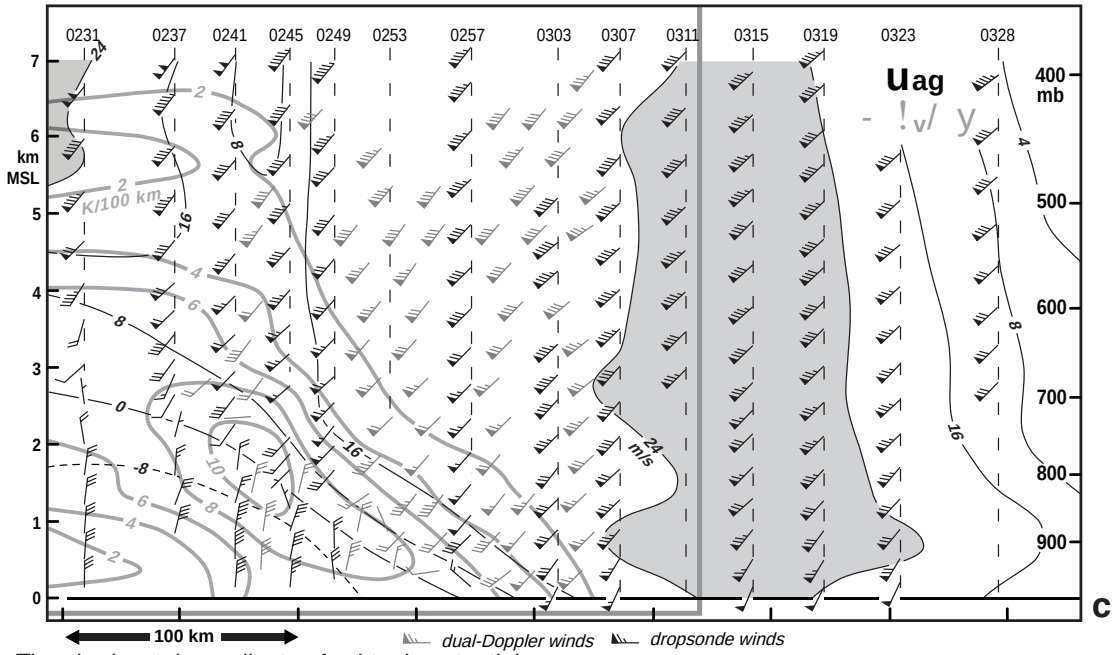

The horizontal gradient of virtual potential temperature across the front is >10 K/100 km with the maximum located aloft at ~2 km (Fig. 4c). This maximum is nearly twice the value near the surface. This is in contrast to the paradigm of the vertical structure of cold fronts where the most intense gradients are located near the surface (e.g., Sanders 1955).

An enlarged view of the precipitation echoes and θ_v analysis superimposed on the dual-Doppler and dropsonde wind field reveals the detailed kinematic structure of the cold front is shown in Fig. 5a. Three bands associated with weak radar reflectivities are noted in the radar reflectivity pattern. Each band is near the regions of positive vertical velocity (Fig. 5b). The band spacing is ~50 km and show a multicellular structure that is typical within a mesoscale convective system with the stronger cells at the leading edge and progressively weaker echoes toward the rear of the system. The

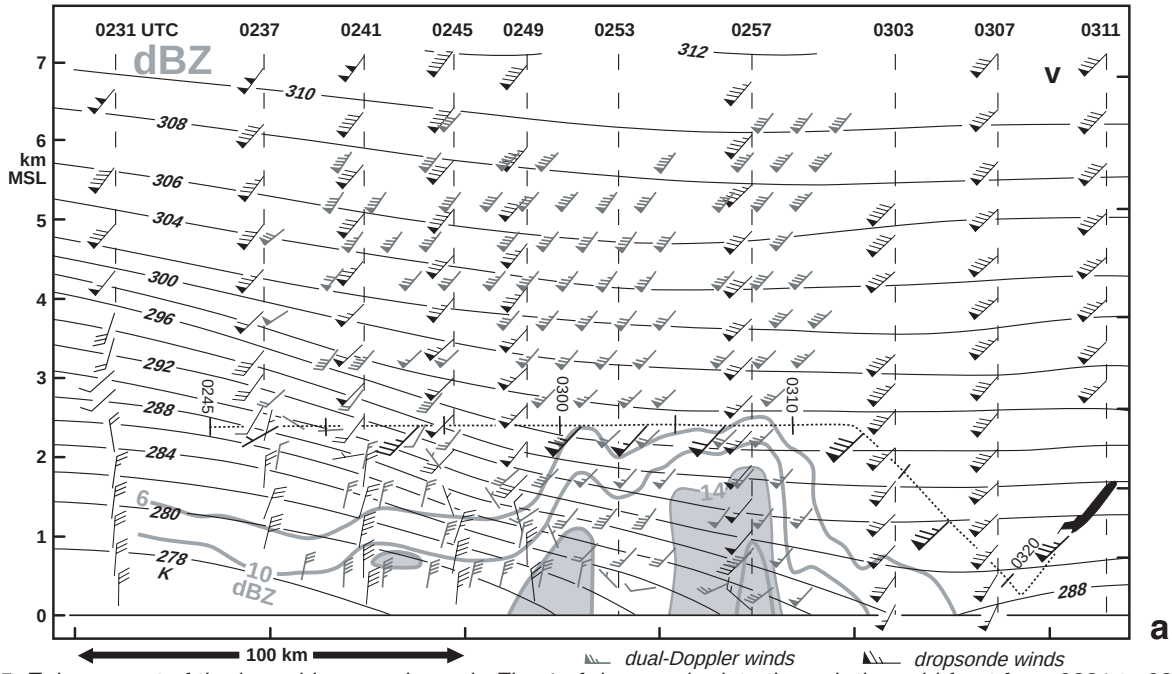

Fig. 5. Enlargement of the boxed-in area shown in Fig. 4 of dropsonde data through the cold front from 0231 to 0328 UTC on 6 February 1997. Ground-relative winds from the dropsondes and Doppler wind synthesis superimposed onto (a) virtual potential temperature and radar reflectivity. (b) vertical vorticity and vertical velocity (dashed-dot line in is the 0.25 x 10^{-3} s^{-1} isopleth of vorticity). (c) virtual potential temperature and cross-frontal potential vorticity defined as $\Phi g \rho f \cdot \partial \Phi E u / E y_s \cdot \partial \Phi E \aleph / E p$, *where* $\partial \Phi E u / E y_s$ *is the cross-frontal vorticity on an isentropic surface and* $\partial E \aleph / E p$, *is the static stability. Black crosses embedded within a circle represent the center of PV couplets. Potential vorticity unit (PVU) = 10^{-6} m^2 s^{-1} K kg^{-1}. (d) tilting and confluence frontogenesis. (e) total frontogenesis and the diabatic term.*

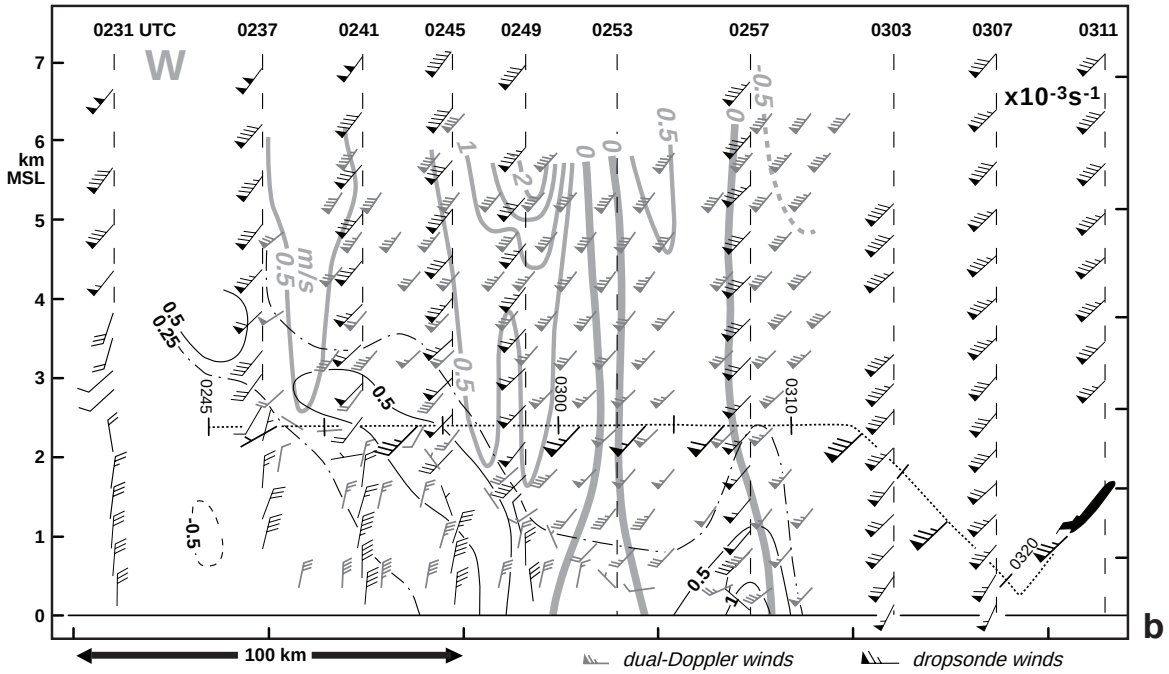

strongest region of cyclonic vertical vorticity (>10^{-3} s^{-1}) is near the surface location of the dropsonde deployed at 0257 (Fig. 5b). The maximum vertical vorticity within the frontal zone (>0.5 x 10^{-3} s^{-1}) does not weaken substantially with increasing height (note the vorticity profile between the 0231 - 0249 soundings). This is also contrary to the commonly accepted paradigm of surface cold fronts.

The relationship between θ_v and potential vorticity (PV) is shown in Fig. 5c. There are several regions within the frontal zone where PV exceeds 2 PVU (potential vorticity units) with the maximum values (>4 PVU) positioned aloft and approximately 50 km behind the leading edge of the front. The location of the maximum is not surprising in light of the increased static stability in this region and the vertical vorticity analysis presented in Fig. 5b. The reverse is true at the location of the surface front where reduced static stability leads to a lower positive value of PV even though the isentropic shear vorticity is a maximum.

There is a suggestion of two PV couplets (highlighted by the black crosses) in the vertical that are positioned near the two updrafts depicted in Fig. 5b. This may be an example of positive and negative PV sources in response to diabatic heating released via condensation in air parcels rising in updrafts. The position and orientation of these couplets in relation to a diabatic heat source is

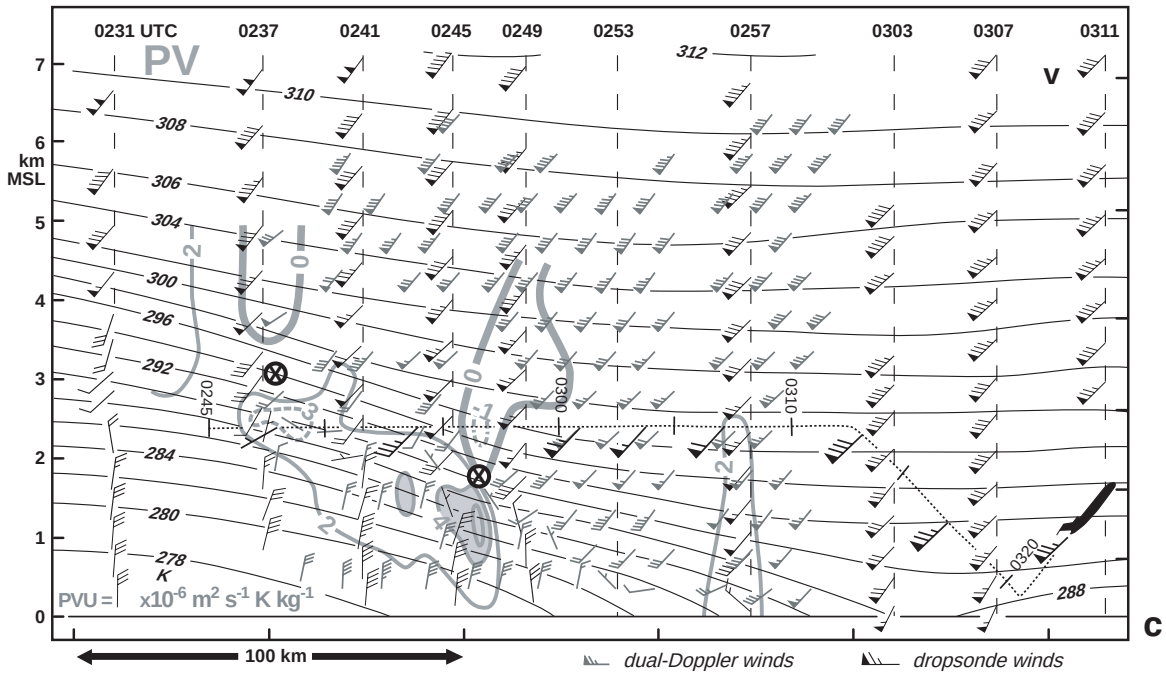

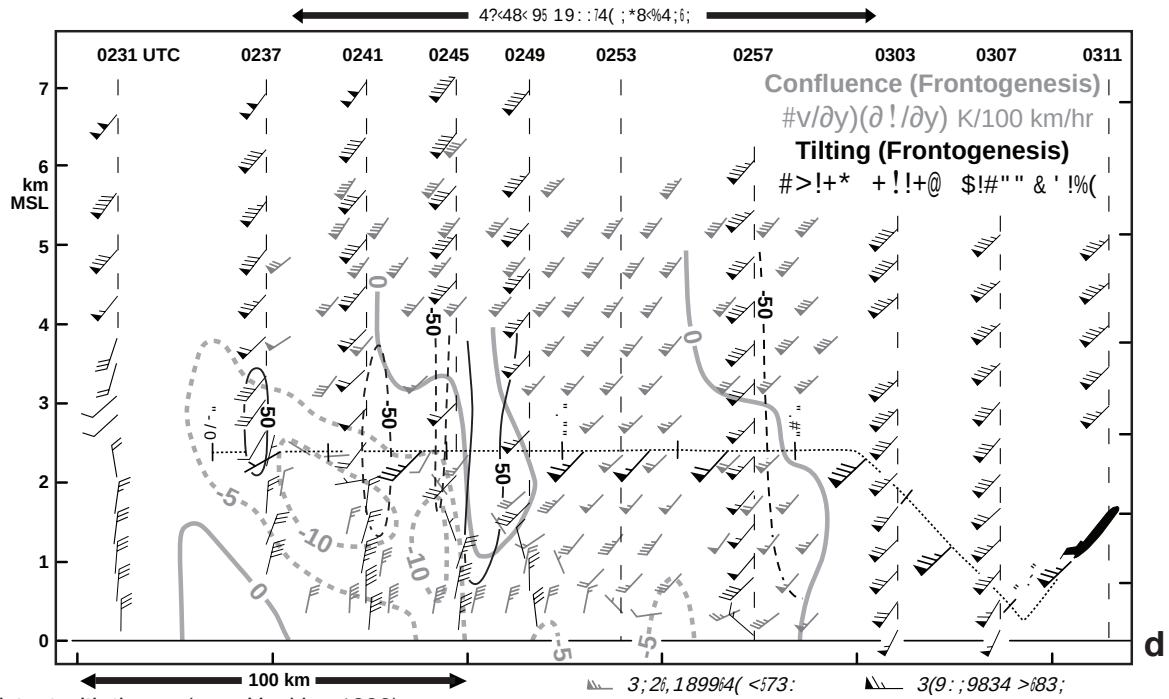

consistent with theory (e.g., Hoskins 1990).

The inviscid form of the frontogenesis equation in two dimensions was used as follows:

$$F = \frac{\partial v}{\partial y}\frac{\partial \theta_v}{\partial y} + \frac{\partial w}{\partial y}\frac{\partial \theta_v}{\partial z} + \Phi\left|\frac{\partial}{\partial y}\right|\left|\frac{d\theta_v}{dt}\right|$$

These terms represent the frontogenetical effects of confluence, tilting and diabatic effects, respectively. There have been few studies that have examined the diabatic term in the frontogenesis equation (e.g., Koch 1984, Keyser 1986, Miller et al. 1996, Neiman et al. 1993, Segal et al. 1993).

The tilting and confluence components of frontogenesis are shown in Fig. 5d. The confluence term is primarily frontolytic with the minimum values located aloft and to the rear of the surface position of the front. The tilting effect is dominant owing to the updrafts and the strong static stability within the frontal zone. The combined effects of tilting and confluence (not shown) reveals weak frontogenesis at the surface location of the front. The diabatic heating can be estimated if it is assumed that the tendency term is negligible and the along-front variations of θ_v are small (Fig. 5e). The cold frontal region is largely associated with diabatic heating primarily through the vertical advective term (i.e., updrafts

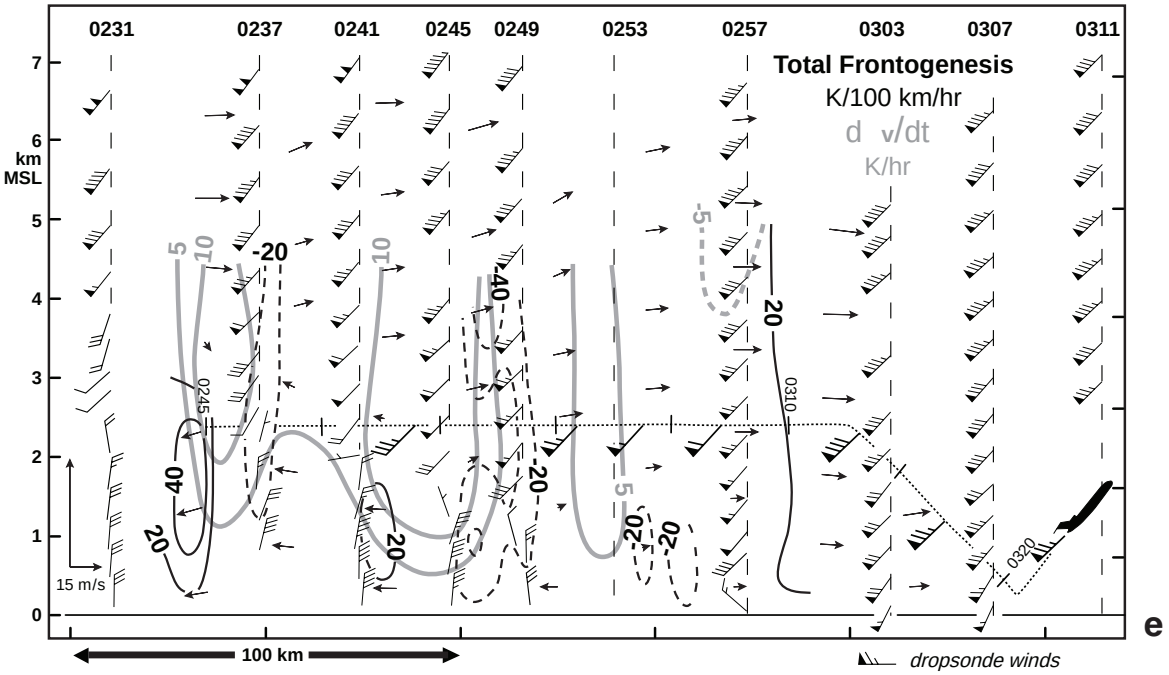

located where the vertical temperature gradients are strong). The two strongest regions of diabatic heating are nearly collocated with the PV couplets (Fig. 5c) which is consistent with the hypothesis that the couplets are a result of a heat source as predicted by theory. This relationship has been rarely shown in observational studies (e.g., Neiman et al. 1993). The combined effects of the tilting, confluence, and diabatic terms is shown in Fig. 5e. In the present case, the diabatic term in the frontogenesis equation was significantly larger than confluence and tilting effects. Accordingly, the analysis is dominated by an alternating pattern of frontogenesis/ frontolysis (Fig. 5e) that is located along the flanks of the maximum of diabatic heating.

5. SUMMARY AND DISCUSSION

Analysis of an oceanic cold front based on airborne Doppler wind syntheses and dropsonde data was presented. The finescale resolution and areal extent of the kinematic and thermodynamic data used in this study is believed to be unprecedented. The front was characterized by a distinct wind shift and horizontal temperature gradient. The latter was most intense aloft which is different from the classical paradigm of cold fronts. In addition, the kinematic discontinuity of the front as quantitatively measured by vertical vorticity did not weaken substantially with increasing height. A dry pocket of descending air was noted out ahead of the front and low-level jet.

The supergeostrophic nature of the upper- and low-level jets was shown based on the observed geopotential height field. Couplets of PV in the vertical were resolved that appeared to be a result of diabatic heat sources in updrafts associated with radar reflectivity cores. This latter relationship has rarely been shown in observational studies. The importance of diabatic effects in the frontogenesis equation was presented. \ In the present case, this diabatic term was dominate easily exceeding the combined effects of confluence and tilting.

Acknowledgements. Research results presented in this paper were partially supported by the National Science Foundation under Grant ATM-021048. The National Center for Atmospheric Research is sponsored by the National Science Foundation. Any opinions, findings and conclusions or recommendations expressed in this publication are those of the authors and do not necessarily reflect the views of the National Science Foundation.

REFERENCE

Bond, N.A., and M.A. Shapiro, 1991: Research aircraft observations of the mesoscale and microscale structure of a cold front over the Eastern Pacific Ocean. *Mon. Wea. Rev.*, **119,** 3080-3094.

Browning, K.A., 1986: Conceptual models of precipitation systems. *Wea. Forecasting*, **1,** 23-41.

_____, and T.W. Harrold, 1970: Air motion and precipitation growth at a cold front. *Quart. J. Roy. Meteor. Soc.*, **96,** 369-389.

Carbone, R.E., 1982: A severe frontal rainband. Part I: Stormwide hydrodynamic structure. *J. Atmos. Sci.*, **39,** 258-279.

Emanuel, K.A., 1983: On assessing local conditional symmetric instability from atmospheric soundings. *Mon. Wea. Rev.*, **111,** 2016-2033.

Gall, R.L., R.T. Williams, and T.L. Clark, 1988: Gravity waves generated during frontogenesis. *J. Atmos. Sci.*, **45,** 2204-2219.

Hobbs, P.V., and K.R. Biswas, 1979: The cellular structure of narrow cold-frontal rainbands. *Quart. J. Roy. Meteor. Soc.*, **105,** 723-727.

_____, and P.O. Persson, 1982: The mesoscale and microscale structure and organization of clouds and precipitation in midlatitude cyclones. Part V: The substructure of narrow cold-frontal rainbands. *J. Atmos. Sci.*, **39,** 280-295.

Hoskins, B.J., 1990: Theory of extratropical cyclones. Extratropical Cyclones, *The Erik Palmén Memorial Volume*, C.W. Newton and E. Holopainen, Eds., Amer. Meteor. Soc., 63-80.

James, P.K., and K.A. Browning, 1979: Mesoscale structure of line convection at surface cold fronts. *Quart. J. Roy. Meteor. Soc.*, **105,** 371-382.

Joly, A., D. Jorgensen, M.A. Shapiro, A. Thorpe, P. Bessemoulin, K.A. Browning, J.-. Cammas, J.-P. Chalon, S.A. Clough, K.A. Emanuel, L. Eymard, R. Gall, P.H. Hildebrand, R.H. Langland, Y. Lemaître, P. Lynch, J. Moore, P.O.G. Persson, C. Snyder, and R.M. Wakimoto, 1997: The Fronts and Atlantic Storm-Track Experiment (FASTEX): Scientific objectives and experimental design. *Bull. Amer. Meteor. Soc.*, **78,** 1917-1940.

Keyser, D., 1986: Atmospheric fronts: An observational perspective. *Mesoscale Meteorology and Forecasting*, P.S. Ray, Ed., Amer. Meteor. Soc., 216-258.

Koch, S.E., 1984: The role of an apparent mesoscale frontogenetic circulation in squall line initiation. *Mon. Wea. Rev.*, **112,** 2090-2111.

Locatelli, J.D., J.E. Martin, and P.V. Hobbs, 1995: Development and propagation of precipitation cores on cold fronts. *Atmos. Res.*, **38,** 177-206.

Miller, L.J., M.A. LeMone, W. Blumen, R.L. Grossman, N. Gamage, and R.J. Zamora, 1996: The low-level structure and evolution of a dry Arctic front over the central United States. Part I: Mesoscale observations. *Mon. Wea. Rev.,* **124,** 1648-1675.

Neiman, P.J., M.A. Shapiro, and L.S. Fedor, 1993: The life cycle of an extratropical marine cyclone. Part II: Mesoscale structure and diagnostics. *Mon. Wea. Rev.*, **121,** 2177-2199.

Ogura, Y., and D. Portis, 1982: Structure of the cold front observed in SESAME-AVE III and its comparison with the Hoskins-Bretherton frontogenesis model. *J. Atmos. Sci.*, **39,** 2773-2792.

Parsons, D.B., and P.V. Hobbs, 1983: The mesoscale and microscale structure and organization of clouds and precipitation in midlatitude cyclones. XI: Comparisons between observations and theoretical aspects of rainbands. *J. Atmos. Sci.*, **40,** 2377-2397.

Sanders, F., 1955: An investigation of the structure and dynamics of an intense surface frontal zone. *J. Meteor.*, **12,** 542-552.

Segal, M., W.L. Physik, J.E. Heim, and R.W. Arritt, 1993: The enhancement of cold-front temperature contrast by differential cloud cover. *Mon. Wea. Rev.*, **121,** 867-873.

Shapiro, M.A., T. Hampel, D. Rotzoll, and F. Mosher, 1985: The frontal hydraulic head: A micro-⁄ scale (~1 km) triggering mechanism for mesoconvective weather system. *Mon. Wea. Rev.*, **113,** 1166-1183.

Wolfsberg, D.G., K.A. Emanuel, and R.E. Passarelli, 1986: Band formation in a New England winter storm. *Mon. Wea. Rev.*, **114,** 1552-1569.

Young, G.S., and R.H. Johnson, 1984: Meso- and microscale features of a Colorado cold front. *J. Climate Appl. Meteor.*, **23,** 1315-1325.